~~Photoelectron Imaging of the Isolated Antimony Tartrate Dianion~~

Photoelectron imaging as a probe of the repulsive Coulomb barrier in the photodetachment of antimony tartrate dianions

*Christopher W. West, James N. Bull, David. A. Woods and Jan R. R. Verlet**

Department of Chemistry, Durham University, Durham, DH1 3LE

Corresponding Author

*j.r.r.verlet@durham.ac.uk

Abstract:

A photoelectron imaging study of the text-book antimony tartrate dianion is presented. The vertical and adiabatic detachment energies are determined to be 2.5±0.1 eV and 2.1±0.2 eV, respectively. The photoelectron spectra exhibit a typical cut-off due to the presence of the repulsive Coulomb barrier (RCB) and the photoelectron images are highly anisotropic. Using a simple model for the RCB combined with classical molecular dynamics simulations, the photoelectron images were calculated and compared with experiment. Very good overall agreement between the simulations and experiments was achieved when the photodetachment occurs along a specific molecular axis. ~~by invoking an anisotropic differential cross section, which correlates the laboratory and molecular frames.~~

KEYWORDS Photoelectron spectroscopy, Multiply charged anion, Polyanions, Repulsive Coulomb barrier, Photoelectron angular distribution

1. Introduction

Multiply charged anions (MCAs) are both common and facile to produce in the solution and solid phases. In contrast, in the gas phase, the lack of a stabilising influence through solvation and other electrostatic interactions, coupled with the strong Coulomb repulsion between the negative charges, tends to destabilise MCAs. Nevertheless, the strong intramolecular Coulomb repulsion also leads to a dynamic stability of MCAs.[1-5] Specifically, the loss of an electron (or anionic fragment) is inhibited by the presence of the so-called repulsive Coulomb barrier[6,7] (RCB), which arises from the long-range repulsion between the electron (fragment) and remaining anion. This dynamic stability can be sufficient to enable the observation of MCAs with a negative electron affinity,[8] in which the ground state lies above that of the detachment threshold. The nature of the RCB can be conveniently probed by photoelectron (PE) spectroscopy.[1,4,6] Only electrons with sufficient kinetic energy to overcome the RCB can be emitted, and this leads to a characteristic cut-off in the PE spectra of MCAs at low energy. Additionally, the outgoing electron is sensitive to the RCB at long-range, which can influence the angular distribution of the emitted PE. Because velocity-map imaging records both the electron kinetic energy (eKE) and the PE angular distribution, PE imaging is ideally suited to studying dianion RCB characteristics.[1,9,10] Highly symmetric molecular MCAs are of particular interest from this perspective as these may be expected to exhibit greater anisotropy. Here, a PE imaging study of antimony tartrate dianion (AT^{2-}, Fig. 1), which is a text-book inorganic dianion salt with high-symmetry (D_2) and a relatively high charge-density, is presented together with simulations of the outgoing PE distribution.

Antimony potassium tartrate has been employed in a variety of applications. The vast majority of historical applications are based around the well-documented toxicity of antimony potassium tartrate and medicinal use.[11-13] Its use in the treatment of alcoholism has also been remarkably persistent, being legally sold for this purpose in the US until the

1940s[14] and reported as recently as 2010.[15] As a gas-phase ion, the majority of studies have been concerned with the accurate determination of antimony in environmental samples, which have been determined by a range of analytical techniques.[16-18] These have included mass-spectrometry and gas-phase absorption spectrum, although, to the best of our knowledge, the gas-phase energetics of AT^{2-} have not been established.

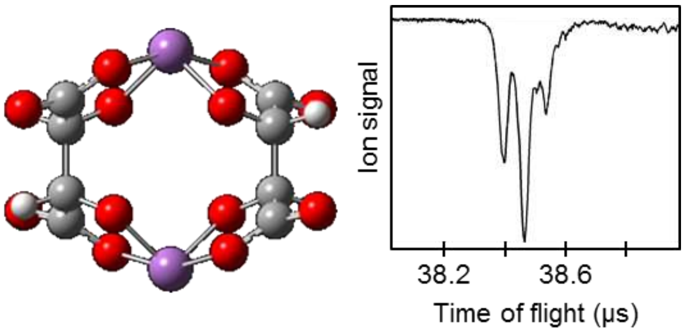

Figure 1: Structure of the antimony tartrate dianion (AT^{2-}) along with its time-of-flight mass spectrum. In the molecular structure Sb is coloured pink, O red, C light grey, and H white.

In the present study, AT^{2-} has been isolated and its PE images recorded at a number of wavelengths. From these data, the electron detachment energetics and the effective height of the RCB in the dianion has been determined. As a representative high-symmetry dianion, AT^{2-} exhibits highly anisotropic PE images. We present classical electron dynamics simulations to describe how the RCB guides the outgoing PE emission, which in turn provides insight into the detachment process. Overall, our results show that the PE angular distribution can be described by classical dynamics provided~~ a suitable connection between the laboratory and molecular reference frames. For AT^{2-} the connection is the differential detachment cross section.~~ that the detachment is taken to be parallel to the molecular *z*-axis.

2. Methodology

The experimental setup and methodology has been previously described in detail.[19,20] Antimony potassium tartrate (Aldrich, 99+ %) was used without further purification. Isolated AT^{2-} was produced by electrospray ionisation of a ~1 mM in MeOH that was coupled to vacuum by a transfer capillary and subsequently trapped in a home-built radio frequency ring-electrode ion trap. The ion packet was pulsed out of the trap at a rate of 10 Hz, mass selected using time-of-flight, and irradiated at the centre of a velocity-map-imaging[21] PE spectrometer,[22] which coincided with the focus of the mass-spectrometer. The isolated AT^{2-} ions were irradiated by nanosecond laser pulses ranging between 3.49 eV (355 nm) and 5.17 eV (240 nm), generated by an optical parametric oscillator (Horizon I, Continuum) pumped by an Nd:YAG laser (Surelite-II, Continuum). The experimental PE images were recorded using a CCD camera that monitored the output of a dual multichannel-plate detector coupled to a phosphor screen. Raw PE images were deconvoluted using the polar-onion peeling algorithm[23] in order to extract the PE spectra and angular distributions. PE spectra were calibrated from the atomic I^- spectrum and have a resolution of ~5%.

Supporting density functional theory (DFT) calculations to characterise geometries and electron detachment energetics were performed at the M06-2X//GEN and M11//GEN levels of theory using the Gaussian 09 software package.[24-26] The GEN basis set includes the aug-cc-pVTZ basis set, although excludes the most diffuse set of *f* and *d* functions for carbon and oxygen atoms, and excludes the most diffuse *d* functions for hydrogen atoms. Antimony was treated with the aug-cc-pVTZ-PP effective core potential basis set.[27] Optimized geometries were confirmed to represent geometrical minima through computation of harmonic vibrational frequencies, which also provided relevant zero-point energy corrections.

3. Results and discussion

3.1 Photoelectron spectroscopy of AT^{2-}

The time-of-flight mass spectrum, shown in Fig. 1, contains a manifold of peaks consisting of a triplet with a ratio of approximately 2:3:1, centred at m/z = 268. The isotopic distribution leading to the observed triplet arises from the natural abundance of Sb. For two Sb ions with ^{121}Sb:^{123}Sb ~ 57:43,[28] the resulting distribution is expected to have a ratio of 1.8:2.6:1, in good agreement with experiment. This manifold of peaks can thus be confidently assigned to AT^{2-}.

Fig. 2 shows the PE spectra of the AT^{2-} dianion collected at 355 nm (3.49 eV), 4.28 eV (290 nm), 4.77 eV (260 nm), and 5.17 eV (240 nm). Also shown are the reconstructed central slices of the full PE distribution. These are obtained from a fit to ~~The top section shows the experimental central slice and the bottom section shows the fit to~~[29,30]

$$I(\theta) \propto 1 + ½(\beta_2 (3 \cos^2\theta - 1)) , \qquad (1)$$

where θ is the angle between the velocity vector of the outgoing PE and the polarisation vector of the light, **ε**. The anisotropy can be quantified using the β_2 parameter (for a single photon process), which spans from +2 to –1 for a $\cos^2\theta$ or $\sin^2\theta$ distribution, respectively. The top section of the images shows the experimental slice through the centre of the electron cloud and the bottom section shows the simulated slice.

All PE spectra show a single peak centred at an electron binding energy (eBE) of ~2.5 eV, which broadens on the high binding energy side with increasing photon energy. From the PE spectra taken at 4.28 eV, 4.77 eV, and 5.17 eV, the vertical detachment energy (VDE) was determined to be VDE = 2.5 ± 0.1 eV and the adiabatic detachment energy (ADE) can be estimated by extrapolation of the low binding energy edge to the value of ADE = 2.1 ± 0.2 eV.

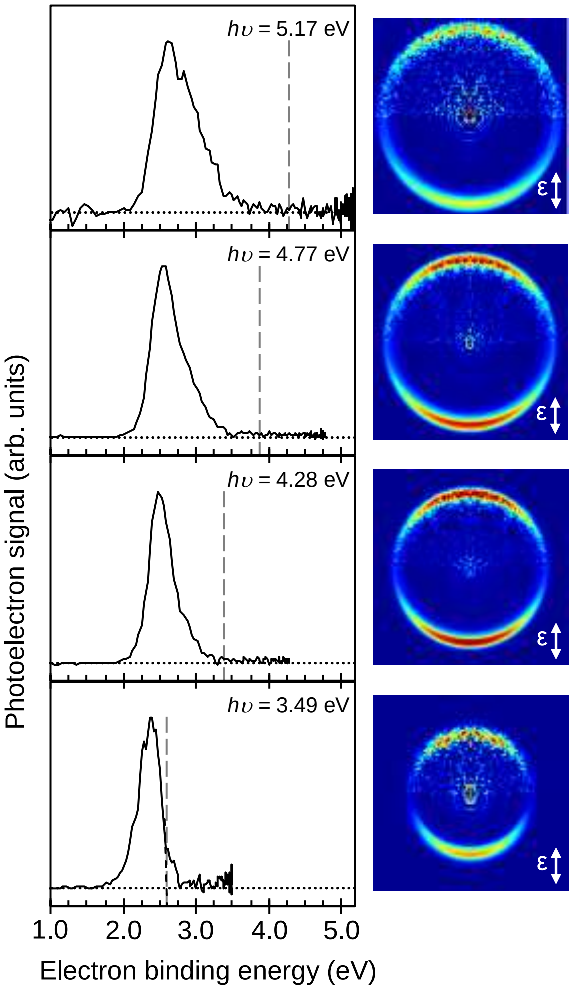

Figure 2: Photoelectron spectra recorded at 5.17 eV (240 nm), 4.77 eV (260 nm), 4.28 eV (290 nm) and 3.49 eV (355 nm). The position of the repulsive Coulomb barrier at each binding energy is indicated by a vertical dashed line. To the right of each spectrum is the corresponding central slice through the experimental (top) and simulated (bottom) velocity-map image. The polarisation vector, **ε**, is indicated by the arrow.

The minimum energy structure of the dianion has D_2 point symmetry (Fig. 1). From the DFT calculations, the VDE was calculated at 2.78 eV (M06-2X functional) or 3.05 eV (M11 functional), while the ADE was calculated at 2.63 eV (M06-2X) and 2.84 eV (M11). In both cases the computed values are some way above those determined experimentally.

Several calculations varying the amount of global Hartree-Fock exchange in the M06 suite of functionals shows the VDE to change between 2.11 eV and 3.91 eV, for 27% and 100% exchange, respectively. This variation simply reflects the inadequacies in DFT and functional parameterization to correctly describe systems of this type. Of note, M06-2X has 54% Hartree-Fock exchange, while M11 is a range-separated functional in which there is 43% local and 100% non-local Hartree-Fock exchange. Despite these variations in electron affinities, population analysis of the charge localization showed a reasonable insensitivity to the specific functional parameterization.

The PE spectrum at 3.49 eV was excluded from the determination of photodetachment energetics as the observed signal levels were orders of magnitude lower because of the close proximity to the top of the RCB.[31] The RCB presents a barrier to photodetachment of MCAs, produced by the competition between short-range attraction and long-range repulsion of a PE and the AT^{-} anion.[1,4] Classically, only electrons with sufficient kinetic energy to surmount the RCB can be detected using PE spectroscopy.[31] Quantum mechanically, excitation near the top of the RCB may lead to electron tunnelling, which leads to PE signal below the RCB cut-off. This contribution becomes particularly pronounced if the excitation energy of the dianion is resonant with an excited state that is situated above the detachment threshold but below the RCB.[1,10,32-35] In AT^{2-}, there are no excited states around 3.5 eV. The proximity of the RCB, however, means that the true VDE is never sampled in the 3.49 eV PE spectrum, and thus shows a spectral maximum that is 0.15 eV less than the PE spectra at higher photon energies.[31] The 3.49 eV PE spectrum allows for an accurate determination of the RCB height by extrapolating the falling edge at the high binding energy side of the peak. This yields a value for the RCB of 0.9 ± 0.1 eV. The position of the RCB has been indicated as a vertical dashed line in the PE spectra in Fig. 2.

The PE images in Fig. 2 show strong anisotropy that is predominantly parallel to the polarisation of the light, **ε**. The β_2 parameters for the PE peak averaged between 2.3 eV < *eBE* < 2.7 eV are +1.32, +1.16 and +0.97 at the photon energies of 4.25 eV, 4.74 eV, and 5.17 eV, respectively.

3.2. Photoelectron emission dynamics simulation

For a singly-charged anion, the PE emission anisotropy is dictated by the quantum interference between outgoing partial waves of the PE.[29,30] While some qualitative insight can be gained through symmetry considerations,[36] the quantitative prediction of the PE angular distribution for large molecular systems remains very difficult.[37,38] In contrast, the PE emission from a dianion is dominated by the long-range RCB and this may be expected to be the determining factor of the experimentally observed PE distribution.[1,9,10] In accord, to a first approximation, photoemission from a dianion can be viewed as a classical electron moving on the RCB of the system. Within this zeroth order picture, the observed anisotropy can be modelled using classical trajectories.

The classical dynamics requires knowledge of the molecular RCB surface, $V(x, y, z)$. This can be calculated using *ab initio* electronic structure methods.[39-41] However, given the known deficiencies of DFT for this system, we approximate $V(x, y, z)$ as the repulsion between an electron and AT^-, where AT^- is modelled as a series of point charges with magnitudes defined as either its Mulliken or natural bond order (NBO) charges.[42] Because electron emission is essentially instantaneous with respect to molecular vibrations, we take AT^- to be in the equilibrium geometry of the dianion. Mulliken or NBO populations indicate that each antimony atom has a charge of +0.9 or +1.9, respectively. The excess negative charge is predominantly distributed across the four carboxylic acid groups (see Fig. 1). The aim of the model here is not to achieve quantitative agreement, but rather to determine if a simple classical picture can capture the observed dynamics and trends. The point-charge model will almost certainly not reproduce the true shape of the RCB at short-range, but should perform better at long-range. It is also important to recognise that the model ignores polarization of AT⁻ by the outgoing electron.

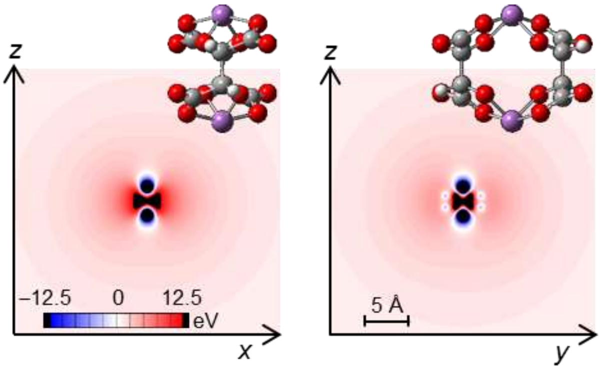

Figure 3: Electrostatic potential energy surface of an electron and the AT⁻ anion in the dianion geometry shown in the *xz* (left) and *yz* (right) planes. The positions of the antimony cations are clearly identifiable by the large attractive (blue) potential wells.

Fig. 3 shows $V(x, y = 0, z)$ and $V(x = 0, y, z)$ on the left and right panes, respectively, calculated using NBO charges (very similar surfaces are generated using Mulliken charges). The Cartesian frame in Fig. 3 is relative to the molecular axes. The shape of $V(x, y, z)$ has two characteristics that are important in determining the observed PE anisotropy. Firstly, there is a large repulsive barrier in the *xy* plane around the molecule which roughly coincides with the location of the tartrate subunits. Secondly, two large attractive wells surround the antimony atoms as these are predominantly cationic in nature. The antimony ions lowers the potential so that the lowest point on the $V(x, y, z)$ (maximum along the saddle point) lies along the molecular *z* axis. Electrons will require less energy to overcome these points and therefore, we anticipate that the PE will be emitted along the *z* axis at low photon energies. The minimum energy barrier (RCB) along the *z* direction was calculated to be 1.1 eV (1.4 eV using Mulliken charges). This value is in good with the experimental RCB value of 0.9 eV

RCB given the severe approximations, especially at short-range, and the limitations of the DFT calculations.

To more completely examine the effect of the RCB on the observed PE anisotropy, the PE images were simulated using the electrostatic potential, $V(x, y, z)$. The simulation invokes the approximation that electron detachment is equivalent to electron attachment. That is, to model the PE trajectories, a PE of a given eKE, initially at some distance from the AT^{-}, is allowed to propagate classically towards the AT^{-}. If the incoming PE has sufficient kinetic energy to overcome the peak of the $V(x, y, z)$ along its trajectory, then there is some probability that this electron trajectory could have been accessed in AT^{2-} photodetachment. In a simple physical picture, the electrons that contribute to the PE spectrum should be those with trajectories that lead to a bound dianion – *i.e.* when $V(x, y, z) < 0$.

To implement the above, a series of random starting positions on a sphere of radius 1000 Å (Coulomb repulsion ~ 0.014 eV) from the centre of the molecule were chosen. From these random positions, the electron was directed to points on a 4×4×4 Å grid in x, y and z around the centre of AT^{-}, and the magnitude of the velocity vector was defined by the chosen eKE. The electrostatic force on the electron at each point was calculated and the electron trajectory was computed according to Newton's equations of motion using the velocity Verlet algorithm.[43,44] A time step (proportional to the inverse square root of the force) was chosen to be sufficiently small to sample the dynamics accurately. The trajectories were continued until the electron either re-crossed the boundary sphere or until the electron reaches a region at which $V(x, y, z) < 0$. We consider that the former electron trajectories do not contribute to the PE emission while the latter do.

In order to relate the simulation to the velocity-mapped PE images, we record the initial velocities of any trajectories that may surpass the RCB. These trajectories have been plotted on the surface of a boundary sphere in Fig. 4 for a range of different eKE. Each panel in Fig. 4 consists of ~1.5×10^4 trajectories.

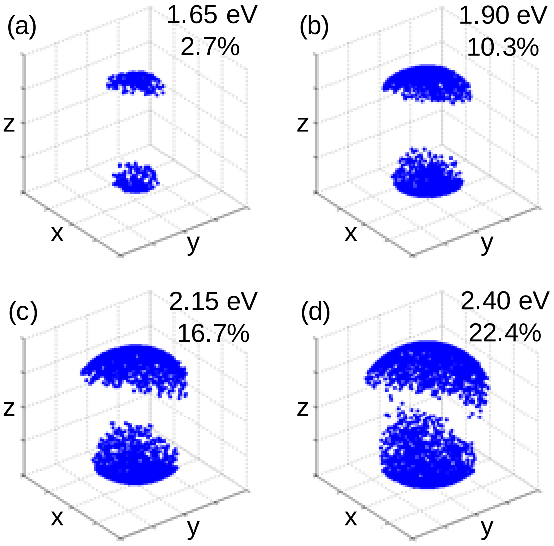

Figure 4: Initial velocities of the simulated electrons at initial kinetic energies of (a) 1.65 eV, (b) 1.90 eV, (c) 2.15 eV, and (d) 2.40 eV. Only the starting positions of electrons that surpass the RCB are shown. The percentage of trajectories that surpass the RCB is also given.

From Fig. 4, it is clear that the initial positions of trajectories of electrons that surpass the RCB are clustered about the *z*-axis. This is in agreement with the expected result based on the shape of $V(x, y, z)$ shown in Fig. 3. Fig. 4(a) shows the results for energies of 0.25 eV above the RCB. Only a small fraction (2.7%) of the electron trajectories contribute to the PE emission, which forms an almost symmetric circle around the *z*-axis. As the kinetic energy is increased, the fraction of trajectories increases to 22.4% for kinetic energies of 1.0 eV in excess of the RCB (Fig. 4(d)). As the eKE increases, the distribution of trajectories that contribute to the PE emission also broadens. This broadening is caused by two factors: (i) the area over which the $V(x, y, z)$ can be overcome increases because the RCB is a saddle point; and (ii) the influence of $V(x, y, z)$ on the trajectory of the incoming (or outgoing) electron decreases as the relative excess kinetic energy increases. Additionally, the anisotropy in $V(x,$

y, *z*) becomes clearly apparent in Fig. 4 as the distribution of PE emission is no longer a symmetric cap around the *z*-axis. This is a direct effect of the geometry of the molecule; the distribution widens over the *x* axis, whereas the tartrate subunits are located over the *y* axis. The presence of the tartrate subunits results in a higher repulsion of the electron from the *y* direction than the *x* axis, resulting in a lower RCB on the *xz* plane than the *yz* plane (see Fig. 3).

The anisotropy plotted in Fig. 4 is not directly comparable with a single-photon PE spectroscopy experiment because the simulations present the molecular-frame (MF) PE angular distribution. In the experiment, the laboratory-frame (LF) distribution is measured and the PE emission is measured from a randomly distributed ensemble of dianions. In order to relate the simulated distributions to the experimentally observed β_2 parameters, the random orientation of AT^{2-} relative to **ε** must be accounted for.

~~If the differential cross section for photodetachment relative to ε was isotropic,~~ If the photodetachment could occur with equal probability along the *z* and *x* (or *y*) molecular axes, then for a random initial distribution of AT^{2-}, one would expect to experimentally observe a perfectly isotropic PE distribution with $\beta_2 = 0$, regardless of any RCB anisotropy.[1] Instead, a large positive β_2 is seen in the experimental PE images (Fig. 2) suggesting ~~a differential cross section peaking~~ that photodetachment preferentially occurs along the molecular *z*-axis. To generate a LF distribution, we convolute our simulated MF distribution with ~~the differential cross section to~~ a photodetachment angular dependence, where the angle θ is defined between **ε** and the molecular *z* axis. Because rotation about ~~the~~ this *z* axis does not change θ, convolution with a uniform distribution about a 2π rotation in the *xy* plane is sufficient. Rotation about the *x* and *y* axes changes θ. The limiting distributions are a $\cos^2\theta$ or $\sin^2\theta$ distribution, which lead to the maximal and minimal experimental β_2 parameters, respectively. These transformations allow direct comparisons with the experimental velocity-map images. For such comparisons, we consider a 1% slice of the initial sphere about the *yz* plane of the simulated distribution from which the β_2 parameters are extracted by fitting the angular intensity to equation (1).

The experimental β_2 parameter at each photon energy is large and positive, suggesting ~~a differential detachment cross section~~ that photodetachment is predominantly parallel to the laser polarisation. We convolute the LF PE angular distribution with Eq. (1) where β_2 now becomes ~~the~~ an anisotropy parameter ~~of the differential detachment cross section~~ to describe the preferential photodetachment axes, denoted β_2'. Using this procedure we find that $\beta_2' = 2$ provides good quantitative agreement with experiment. The results of the simulations using the Mulliken charges are shown in Fig. 5 together with the experimental β_2 values. To aid comparison between experiment and simulation, the β_2 parameters have been plotted as a function of the electron's kinetic energy in excess of the RCB. The experimental β_2 parameters are shown at several selected energies spanning the PE distribution (where PE signal is greater than half of the peak – see Fig. 2) for four different photon energies. At the lowest photon energy, the β_2 data is noisy which reflects the close proximity to the RCB cut-off where the signal levels were very low. Similarly, at the highest photon energy (5.17 eV), noise increases because of the increase in background electrons in our experiment.

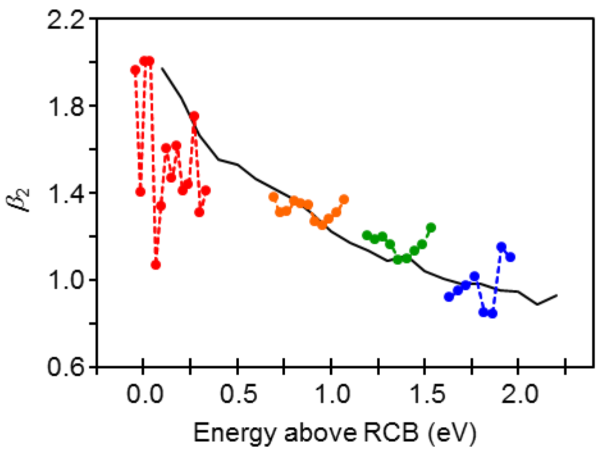

Figure 5: Comparison between β_2 parameters obtained by fitting the central plane of an electron distribution extracted from the simulation (black line) using the Mulliken charges and the β_2 parameters extracted from the photoelectron images (circles, dashed line) taken at 3.49 eV (red), 4.28 eV (orange), 4.77 eV (green) and 5.17 eV (blue).

The simulation results for the Mulliken and NBO charges are very similar, suggesting that, even though the localised partial charges vary between both methods and the absolute RCB heights differ by ~0.3 eV, the overall shape of the Coulomb potential is very similar, especially at long-range. Any differences in the calculated electron trajectories due to the differences in the point charges are expected to be most prominent at short-range. Thus, the similarity of the final PE angular distributions for both methods supports the contention that the experimental PE distributions are dominated by long-range Coulomb interactions. That the experimental β_2 values decrease with increasing excess kinetic energy is reproduced in the simulations. Furthermore, the rate of decrease in β_2 with increasing energy above the RCB is also reproduced reasonably well, suggesting that the simple classical model has captured the underlying physics.

The surprisingly good agreement between simulation and experiment suggests that some of the major deficiencies in the model may not be as severe as might be anticipated. The simplistic potential, based on localised fractional point charges, has singularities at the atomic sites and will have potential gradients that are too steep in the immediate proximity of these sites. However, lower photon energies are unable to create electrons that have trajectories that sample the immediate vicinities of these sites. In addition, polarisation of the molecular orbitals of AT^- by the incoming electron may influence the charge distribution and therefore the gradient of β_2 as a function of energy. Although it is completely ignored, based on the overall agreement between simulation and experiments, this polarisation does not seem to be too important in this case. We have also assumed a constant β_2' value across the energy range. In reality, one might anticipate β_2' to have a modest energy dependence. We note that if ~~neutral~~ excited states of AT^- were to become available with increasing photon energy, sudden changes in β_2' might be expected, although is not the case here. Finally, we also stress that the model is purely classical and all quantum interference effects have been ignored. The agreement in Fig. 5 therefore suggests that the PE angular distributions measured in experiments are predominantly dictated by the long-range classical interaction of the RCB and outgoing PE.

In summary, the simulation results support the contention that classical dynamics dominate the PE angular distributions of dianions.[1,9,10] To observe PE anisotropy ~~form~~ from a dianion (or any MCA), we emphasise that a connection is needed between the LF and MF. In the present case, this connection is provided by a ~~very anisotropic differential photodetachment cross section~~ strong preference for photodetachment along the molecular *z* axis ($\beta_2' = +2$). However, in general, ~~the differential photodetachment cross section~~ this preference is not known *a priori* so that the observed PE anisotropy can be difficult to interpret. A route to enable more direct comparisons would be by pre-alignment the dianion before photodetachment, for example, using resonant excitation if the dianion supports a bound electronic excited state.[10,45] However, even in such a case, knowledge of the ~~differential cross section for~~ photodetachment alignment from the excited state is still required.

4. Conclusion

A PE imaging study of the text-book antimony tartrate dianion ionic complex has been presented at a number of wavelengths. The vertical and adiabatic detachment energy were determined to be 2.5 ± 0.1 and 2.1 ± 0.2 eV, respectively. The PE spectra show the expected cut-off due to the RCB, from which the height has been determined to be 0.9 ± 0.1

eV. All PE images are highly anisotropic. DFT calculations provided the equilibrium structure of AT^{2-} and partial charges on each atom in AT^{-} as either Mulliken or NBO populations. The full RCB potential energy surface was then calculated using a simple model of an electron in the electrostatic field of AT^{-} point charges assuming the AT^{2-} geometry. The surface indicates that the RCB is highly anisotropic and would result in electron emission predominantly along the Sb–Sb axis (*z*-axis). The PE images were simulated using classical dynamics of an electron on the RCB surface and compared to experiment. This showed that good agreement was attainable ~~assuming a differential cross section peaking along~~ by noting a strong preference for photodetachment along the molecular *z*-axis. The simulations broadly reproduced the observed changes of PE anisotropy as a function of the electron's kinetic energy. The agreement between experiment and this simple model reflects that the PE angular distributions of a dianion are likely dominated by the long-range Coulomb interaction of the outgoing electron and the remaining anion. The results also highlight that knowledge of the relationship between laboratory and molecular frames is essential to correctly characterize such effects.

Acknowledgements

Funding was provided by the ERC (Starting Grant 306536). The Durham Chemistry Teaching Laboratories are thanked for providing the Antimony Potassium Tartrate sample and the previous Undergraduates are thanked for failing to use it up.

References

(1) Chatterley, A. S.; Horke, D. A.; Verlet, J. R. R. *Phys. Chem. Chem. Phys.* **2014**, *16*, 489.

(2) Dreuw, A.; Cederbaum, L. S. *Chem. Rev.* **2002**, *102*, 181.

(3) Scheller, M. K.; Compton, R. N.; Cederbaum, L. S. *Science* **1995**, *270*, 1160.

(4) Wang, X.-B.; Wang, L.-S. In *Ann. Rev. Phys. Chem.*; Annual Reviews: Palo Alto, 2009; Vol. 60, p 105.

(5) Wang, L.-S. *J. Chem. Phys.* **2015**, *143*, 040901.

(6) Wang, X.-B.; Ding, C.-F.; Wang, L.-S. *Phys. Rev. Lett.* **1998**, *81*, 3351.

(7) Simons, J.; Skurski, P.; Barrios, R. *J. Am. Chem. Soc.* **2000**, *122*, 11893.

(8) Wang, X.-B.; Wang, L.-S. *Nature* **1999**, *400*, 245.

(9) Xing, X.-P.; Wang, X.-B.; Wang, L.-S. *Phys. Rev. Lett.* **2008**, *101*, 083003.

(10) Horke, D. A.; Chatterley, A. S.; Bull, J. N.; Verlet, J. R. R. *J. Phys. Chem. Lett.* **2012**, *3*, 834.

(11) Winship, K. A. *Adverse Drug React. Acute Poisoning Rev.* **1987**, *6*, 67.

(12) Sundar, S.; Chakravarty, J. *Int. J. Environ. Res. Public Health* **2010**, *7*, 4267.

(13) Winslow, F. *J. Psych. Med. Mental Path.* **1857**, *10*, 1.

(14) In *United States v. 11 1/4 Dozen Packages Labeled in Part 'Mrs. Moffat's Shoo Fly Powders for Drunkenness'*; Dist. Court, WD New York: 1941; Vol. 40, p 208.

(15) Konstantopolous, W. M.; Ewald, M. B.; Pratt, D. S. *N. Engl. J. Med.* **2012**, *367*, 259.

(16) Filella, M.; Belzile, N.; Chen, Y.-W. *Earth Science Reviews* **2002**, *57*, 125.

(17) Smichowski, P. *Talanta* **2008**, *75*, 2.

(18) Wilson, S. C.; Lockwood, P. V.; Ashley, P. M.; Tighe, M. *Environ. Pollut.* **2010**, *158*, 1169.

(19) Horke, D. A.; Verlet, J. R. R. *Phys. Chem. Chem. Phys.* **2011**, *13*, 19546.

(20) Lecointre, J.; Roberts, G. M.; Horke, D. A.; Verlet, J. R. R. *J. Phys. Chem. A* **2010**, *114*, 11216.

(21) Eppink, A. T. J. B.; Parker, D. H. *Rev. Sci. Instrum.* **1997**, *68*, 3477.

(22) Horke, D. A.; Roberts, G. M.; Lecointre, J.; Verlet, J. R. R. *Rev. Sci. Instrum.* **2012**, *83*, 063101.

(23) Roberts, G. M.; Nixon, J. L.; Lecointre, J.; Wrede, E.; Verlet, J. R. R. *Rev. Sci. Instrum.* **2009**, *80*, 053104.

(24) Kendall, R. A.; Dunning Jr., T. H.; Harrison, R. J. *J. Chem. Phys.* **1992**, *96*, 6796.

(25) Frisch, M. J.; Trucks, G. W.; Schlegel, H. B.; Scuseria, G. E.; Robb, M. A.; Cheeseman, J. R.; Scalmani, G.; Barone, V.; Mennucci, B.; Petersson, G. A.; Nakatsuji, H.; Caricato, M.; Li, X.; Hratchian, H. P.; Izmaylov, A. F.; Bloino, J.; Zheng, G.; Sonnenberg, J. L.; Hada, M.; Ehara, M.; Toyota, K.; Fukuda, R.; Hasegawa, J.; Ishida, M.; Nakajima, T.; Honda, Y.; Kitao, O.; Nakai, H.; Vreven, T.; Montgomery Jr., J. A.; Peralta, J. E.; Ogliaro, F.; Bearpark, M. J.; Heyd, J.; Brothers, E. N.; Kudin, K. N.; Staroverov, V. N.; Kobayashi, R.; Normand, J.; Raghavachari, K.; Rendell, A. P.; Burant, J. C.; Iyengar, S. S.; Tomasi, J.; Cossi, M.; Rega, N.; Millam, N. J.; Klene, M.; Knox, J. E.; Cross, J. B.; Bakken, V.; Adamo, C.; Jaramillo, J.; Gomperts, R.; Stratmann, R. E.; Yazyev, O.; Austin, A. J.; Cammi, R.; Pomelli, C.; Ochterski, J. W.; Martin, R. L.; Morokuma, K.; Zakrzewski, V. G.; Voth, G. A.; Salvador, P.; Dannenberg, J. J.; Dapprich, S.; Daniels, A. D.; Farkas, Ö.; Foresman, J. B.; Ortiz, J. V.; Cioslowski, J.; Fox, D. J.; Gaussian, Inc.: Wallingford, CT, USA, 2009.

(26) Peverati, R.; Truhlar, D. G. *J. Phys. Chem. Lett.* **2011**, *2*, 2810.

(27) Peterson, K. A. *J. Chem. Phys.* **2003**, *119*, 11099.

(28) Haynes, W. M.; Lide, D. R. *CRC Handbook of Chemistry and Physics: A Ready-Reference Book of Chemical and Physical Data*; 94 ed.; Fla: CRC: Boca Raton, 2010.

(29) Zare, R. N. *Mol. Photochem.* **1972**, *4*, 1.

(30) Reid, K. L. *An. Rev. Phys. Chem.* **2003**, *54*, 397.

(31) Wang, X.-B.; Ding, C.-F.; Wang, L.-S. *Chem. Phys. Lett.* **1999**, *307*, 391.

(32) Chatterley, A. S.; Horke, D. A.; Verlet, J. R. R. *Phys. Chem. Chem. Phys.* **2012**, *14*, 16155.

(33) Horke, D. A.; Chatterley, A. S.; Verlet, J. R. R. *Phys. Rev. Lett.* **2012**, *108*, 083003.

(34) Dau, P. D.; H.-T., L.; Yang, J.-P.; Winghart, M.-O.; Wolf, T. J. A.; Unterreiner, A. N.; Weis, P.; Miao, Y.-R.; Ning, C.-G.; Kappes, M. M.; Wang, L.-S. *Phys. Rev. A* **2012**, *85*, 064503.

(35) Winghart, M.-O.; Yang, J.-P.; Kuehn, M.; Unterreiner, A.-N.; Wolf, T. J. A.; Dau, P. D.; Liu, H.-T.; Huang, D.-L.; Klopper, W.; Wang, L.-S.; Kappes, M. M. *Phys. Chem. Chem. Phys* **2013**, *15*, 6726.

(36) Sanov, A. *Ann. Rev. Phys. Chem.* **2014**, *65*, 341.

(37) Oana, C. M.; Krylov, A. I. *J. Chem. Phys.* **2009**, *131*, 124114.

(38) Liu, Y.; Ning, C. *J. Chem. Phys.* **2015**, *143*, 144310.

(39) Horke, D. A.; Chatterley, A. S.; Verlet, J. R. R. *J. Chem. Phys.* **2013**, *139*, 084302.

(40) Dreuw, A.; Cederbaum, L. S. *Phys. Rev. A* **2001**, *63*, 049904.

(41) Ning, C.-G.; Dau, P. D.; Wang, L.-S. *Phys. Rev. Lett.* **2010**, *105*, 263001.

(42) Reed, A. E.; Curtiss, L. A.; Weinhold *Chem. Rev.* **1988**, *88*, 899.

(43) Verlet, L. *Phys. Rev.* **1967**, *159*, 98.

(44) Verlet, L. *Phys. Rev.* **1968**, *165*, 201.

(45) Horke, D. A.; Chatterley, A. S.; Bull, J. N.; Verlet, J. R. R. *J. Phys. Chem. Lett.* **2015**, *6*, 189.